Graphenelike surface boron layer: Structural phases on transition-metal diborides (0001)

Shigeru Suehara（末原茂), Takashi Aizawa（相澤俊), and Taizo Sasaki（佐々木泰造)
National Institute for Materials Science, 1-1 Namiki, Tsukuba, Ibaraki 3050044, Japan
(Received 25 August 2009; revised manuscript received 22 January 2010; published 19 February 2010)

We have identified two structure phases for a surface boron layer on transition-metal diborides $ZrB_2(0001)$ and $NbB_2(0001)$ using first-principles calculations. Surface-formation free-energy calculations of various surface structures combined with preliminary molecular-dynamics simulations revealed that, in a boron-rich condition, the well-known 1×1 graphitic boron layer (*boraphene*) and $\sqrt{3}\times\sqrt{3}(R\pm30°)(\sqrt{3})$ boraphene are, respectively, thermodynamically more favorable surfaces than the 1×1 metal-terminated surfaces of $NbB_2(0001)$ and $ZrB_2(0001)$. The origin of the $\sqrt{3}$ and 1×1 boraphene surface stability is discussed herein from the electronic-structure perspective. Full-phonon calculations based on the density-functional perturbation theory for these surfaces as well as for ZrB_2, NbB_2, α-B, Zr, and Nb bulk crystals were also performed. The calculated phonon dispersions of the $\sqrt{3}$ and 1×1 boraphenes show excellent agreement with the experimental surface-phonon dispersions. Using phonon energy and electronic density of states of these surface and bulk systems with the harmonic approximation and the Sommerfeld theory, we obtained stable phases of the $ZrB_2(0001)$ and $NbB_2(0001)$ surfaces at each temperature. The calculated phase diagrams show that the thermodynamically favorable region of the boraphene surfaces slightly extends with increasing temperature in these transition-metal diboride surfaces.

DOI: 10.1103/PhysRevB.81.085423 PACS number(s): 68.35.Md, 02.70.−c, 05.70.Np, 63.20.D−

I. INTRODUCTION

Unique features of high hardness, high melting point, and (semi)metallic conductivity or superconductivity are exhibited by AlB_2-type metal diborides.[1–3] These materials consist of alternate stacking of a close-packed metal layer and a planar layer of sp^2-bonded boron atoms. The boron layer forms a two-dimensional honeycomb lattice isostructure with graphene, which has recently attracted considerable attention.[4–8] Therefore, the boron layer can be designated as *boraphene* as an analogous and postgraphene substance. Boraphene is unlikely to be prepared as a free-standing sheet, differently from graphene or a one-atom-thick BN sheet,[9] because it lacks one electron per atom to form the complete sp^2-bond network by itself. In other words, in the AlB_2-type metal diborides, electron donation from the metal layer is expected to make the boraphene sheet stable.

A stability boundary of boraphene can be found in transition-metal diboride (TMB_2)(0001) surfaces. At an ideal 1×1 boraphene surface, the boron atoms lose half of the neighboring metal atoms. This loss is expected to reduce the electron donation compared to that in the bulk. In fact, stable surfaces have been observed[10–13] depending on a TM atom, such as the boraphene surface for $TaB_2(0001)$ and $NbB_2(0001)$, although 1×1 TM metal surfaces are observed for $HfB_2(0001)$ and $ZrB_2(0001)$ under a typical surface treatment. These observations suggest that boraphene is unstable in these group-IV $TMB_2(0001)$ surfaces. To elucidate features of the $TMB_2(0001)$ surfaces, several theoretical works have been undertaken, and energetically favorable surfaces have been discussed.[14,15] Results of those studies imply that a group-IV(V) $TMB_2(0001)$ surface is terminated with a 1×1 TM(B) layer. That is, the stability boundary of the boraphene sheet might be associated with one valence-charge difference between group-IV and group-V TM atoms within a simple picture.

For elucidating these surfaces further, we have studied the $ZrB_2(0001)$ and $NbB_2(0001)$ surfaces experimentally as prototypes that, respectively, exhibit 1×1 boraphene and metal surfaces.[13,16] These materials are known to be metallic as bulk materials with high melting points of 3313 K (ZrB_2) and 3173 K (NbB_2).[17] In addition to the 1×1 metal-terminated surface on the $ZrB_2(0001)$, we recently observed $\sqrt{3}\times\sqrt{3}$ ($R\pm30°$) (hereinafter $\sqrt{3}$) periodicity on this surface in a B-rich condition.[18] Considering the simple picture of the stable surface described above, the structure of the $\sqrt{3}$ phase, which has not been determined, must be understood in a different way.

In this paper, we report the surface formation of two boraphene types: well-known 1×1 graphitic and newly discovered $\sqrt{3}$ phases on $TMB_2(0001)$ (TM=Nb,Zr) using first-principles calculations of electronic structures and vibrational properties based on the density-functional theory.[19,20] We demonstrate that full phonon calculations based on the density-functional perturbation method[20] account excellently for the phonon-dispersion measurements using high-resolution electron-energy-loss spectroscopy (HR-EELS) (Refs. 13 and 18) and discuss the origin of boraphene surface stability from an electronic-structure perspective. The temperature dependence of the surface phases of $TMB_2(0001)$ is also presented.

II. CALCULATION METHODS

A. Grand canonical ensemble approach

We consider a surface adsorption system with possible surface composition controlled in the experiment, where boron atoms are deposited on a $TMB_2(0001)$ substrate in a vacuum. Such an open system is typically described using a grand canonical ensemble. In the following, we map our surface models consisting of a various numbers of atoms on to

the grand canonical ensemble with chemical potentials and temperature. In our calculations, a slab of $TMB_2(0001)$ with a vacuum layer was used as a unit cell in a three-dimensional periodic boundary condition, in which both surfaces of the slab have identical structures. To compare the slab models consisting of various number of atoms, a grand potential was used as the surface-formation free energy,[19] defined as

$$\gamma = \left(F - \sum_i n_i \mu_i \right) / 2, \tag{1}$$

where F signifies the Helmholtz free energy of the system in which n_i atoms of i (i=TM,B) with a chemical potential μ_i are involved. The factor 1/2 accounts for two equivalent surfaces in the slab model.

We approximate F at an absolute temperature T as

$$F(T) = E + F^{el}(T) + F^{ph}(T), \tag{2}$$

where E is the static lattice energy of the system. Also, F^{el} and F^{ph} signify the free-energy contributions of electron and phonon, respectively. In the Sommerfeld theory[21] and harmonic approximation,[22] F^{el} and F^{ph} are expressed as $F^{el}(T) = -\frac{\pi^2}{6} D(\epsilon_f)(k_B T)^2$ and $F^{ph}(T) = k_B T \Sigma_s \ln(2 \sinh \frac{\hbar \omega_s}{2 k_B T})$, where $D(\epsilon_f)$ is the electronic density of states (DOS) at the Fermi level (ϵ_f) and ω_s denotes a phonon frequency of mode s.

Defining $\mu_B^{bulk}(T)$, $\mu_{TM}^{bulk}(T)$, and $\mu_{TMB_2}^{bulk}(T)$ as free energies of the respective bulks (per atom or formula unit), conditions of no precipitation of B or TM on the TMB_2 surface lead to $\mu_B \leq \mu_B^{bulk}(T)$ and $\mu_{TM} \leq \mu_{TM}^{bulk}(T)$. The TMB_2 surfaces in equilibrium with TMB_2 bulk substrate give $2\mu_B + \mu_{TM} = \mu_{TMB_2}^{bulk}(T)$. Furthermore, $\mu_{TMB_2}^{bulk}(T)$ can be associated with the heat of formation $\Delta H_f(T)$ as $\mu_{TMB_2}^{bulk}(T) = 2\mu_B^{bulk}(T) + \mu_{TM}^{bulk}(T) - \Delta H_f(T)$. Because we consider the surfaces by the B atom deposition in the experiment, it is convenient to retain μ_B and T as the system-specifying external parameters. Then, we obtain $-\frac{1}{2}\Delta H_f(T) \leq \Delta\mu_B \leq 0$, where $\Delta\mu_B = \mu_B - \mu_B^{bulk}(T)$. In that equation, $\Delta\mu_B = 0$ and $-\frac{1}{2}\Delta H_f(T)$, respectively, denote B-rich and TM-rich limits.

B. Preconditioning of convergence parameters

All first-principles calculations with the Perdew-Wang 91 gradient-corrected functional[23] were performed using the QUANTUM-ESPRESSO package.[24] Vanderbilt-type pseudopotentials[25] generated by setting the valence configurations of $2s^2 2p^1$, $4s^2 4p^6 4d^2 5s^2$, and $4s^2 4p^6 4d^4 5s^1$ for B, Zr, and Nb, respectively, were used. Computational parameters, such as cut-off energies of plane wave (E_{cut}), quantities of $\boldsymbol{k}$-point sampling in the full Brillouin zone (BZ) in the Monkhorst-Pack (MP) scheme,[26] were determined to establish total-energy convergence of less than 1 mRy/atom. A charge-density cutoff of $6 \times E_{cut}$ and an electronic-state smearing width of 20 mRy by the Marzari-Vanderbilt-type broadening method[27] offered acceptable convergence with respect to total electronic energies.

Optimized structures of ZrB_2, NbB_2, α-B, Zr, and Nb bulk crystals were obtained with residual stress of <0.5 kbar and forces acting on the atoms of $<10^{-4}$ Ry/a.u. In a slab calculation for the $TMB_2(0001)$ surfaces, similar criteria were applied, but the quantities of the $\boldsymbol{k}$-point samplings were reduced based on their cell parameters. A 1×1 slab model consisting of ≥ 7 layers of TM and B with a ≥ 0.7 nm vacuum-layer thickness exhibited sufficient convergence, judging from the total energy and the optimized interlayer distances. Consequently, $6^2 \times 1$ and $9^2 \times 1$ $\boldsymbol{k}$-point samplings were used, respectively, here for $\sqrt{3}$ slab models of $ZrB_2(0001)$ and $NbB_2(0001)$.

C. Molecular-dynamics simulations

In advance of constructing the initial surface structure models for the unknown ZrB_2 (0001)-$\sqrt{3}$ surface, we have done preliminary structure optimization using first-principles molecular-dynamics (MD) simulations of the $ZrB_2(0001)$ 3×3 surfaces, which are of three times larger area than the $\sqrt{3}$ surface, with the seven layers of TM and B and the approximately 1.8-nm-thick vacuum layer. Each MD simulation started at the atomic positions for the bulk. These preliminary MD simulations were undertaken to determine the qualitative behavior of the surfaces at a high temperature and to infer the most probable $\sqrt{3}$ surface structure. Therefore, a coarse calculation condition of only Γ ($\boldsymbol{k}=0$) sampling with 40 mRy of the smearing width was used. An MD time step of 2.9 fs was determined judging from a highest phonon frequency (i.e., quickest motion of atoms) of the bulk. After about 2 ps annealing at temperature of 2500 K controlled by scaling the total kinetic energy of the atoms at every time step, the 3×3 slabs were quenched at a rate of $1.67T \times 10^{-3}$ K/fs (typically about 2000 K/ps).

D. $\sqrt{3}$ slab models

For robust calculation of the surface-formation free energy, we used nine-layer $\sqrt{3}$ slab models with a vacuum layer of approximately 1.8 nm as the $TMB_2(0001)$ metal or boron surfaces on which B and/or TM atoms were attached to form possible structures. It is worth noting that the surface models were first screened using the surface-formation free energy (γ_0) without the energetically minor terms of F^{el} and F^{ph} in Eq. (2) to avoid time-consuming phonon calculations of unlikely surface models.

Over 60 initial surface models, such as simple surface models with B and/or Zr adatom(s) on hollow, bridge, top, or lower symmetric sites, and B dimer(s) and/or trimer(s) adsorbed ones, were evaluated for the $ZrB_2(0001)$-$\sqrt{3}$ surface. In addition, models with defects in the second layers were examined, although results of the preliminary MD simulation suggested that surface reconstruction occurs by the surface boron atoms only as described later in Sec. III B.

E. Phonon dispersion

Full-phonon calculations were performed using the density-functional perturbation theory.[20] The phonon dispersions were drawn, assisted by interpolation techniques[20] based on the interatomic force constants derived from calculated phonon frequencies at specified $\boldsymbol{q}$ points on the MP grid. Numbers of the sampling $\boldsymbol{q}$ points used for the bulk crystals are listed in Table I.

TABLE I. Calculated results (cal) for bulk models: optimized cell parameters a(pm), c(pm), and α(deg), heat of formation ΔH_f (KJ/mol), entropy S (J/mol K), and specific heat at constant volume C_v (J/mol K) at 298.15 K. Available experimental values (exp) are shown for comparison. Applied computational parameters are also listed: cut-off energy of plane wave E_{cut} and the numbers of $\boldsymbol{k}$- and $\boldsymbol{q}$-sampling points in the full Brillouin zone, respectively, for electronic and phonon states.

	ZrB_2		NbB_2		α-B		Zr		Nb
Lattice type	Hexagonal		Hexagonal		Rhombohedral		hcp		bcc
Cell parameter	a	c	a	c	a	α	a	c	a
Cal	316.84	354.34	310.52	333.14	504.01	58.104	322.66	515.45	330.54
Exp	317.0	353.3[a]	310.7	328.2[b]	506.43	58.0962[c]	323.31	514.80[d]	330.00[e]
ΔH_f^{cal}	290.4		208.1						
ΔH_f^{exp}	305.4,[f] 322.59[g]		175.3,[f] 197[h]						
S^{cal}	35.016		38.809		5.3878		38.807		34.917
S^{exp}	35.94[f]		37.49[f]		5.90[i]		39.0[i]		36.4[i]
C_v^{cal}	47.655		48.244		10.915		23.875		23.757
C_p^{exp} [k]	47.78,[j] 48.24[f]		48.12[f]		11.1[i]		25.4[i]		24.6[i]
E_{cut} (Ry)	24		32		24		24		34
$\boldsymbol{k}$ points	$10^2\times 9$		$16^2\times 15$		6^3		$16^2\times 10$		16^3
$\boldsymbol{q}$ points	3^3		3^3		3^3		$4^2\times 3$		6^3

[a]Reference 28.
[b]Reference 17.
[c]Reference 29.
[d]Reference 30.
[e]Reference 31.
[f]Reference 32.
[g]Reference 33.
[h]Reference 34.
[i]References 35 and 36.
[j]Reference 37.
[k]At constant pressure.

In phonon calculations of the optimized slab models, the vacuum-layer thickness was decreased safely to about 0.9 nm to speed up the convergence of each calculation. The sampling $\boldsymbol{q}$-point numbers were $2^2\times 1$ and $3^2\times 1$, respectively, for the $\sqrt{3}$ and 1×1 surface models.

III. RESULTS AND DISCUSSION

A. Bulk properties

Table I presents the calculated results for bulk properties compared with available experimental values: cell parameters, heats of formation ΔH_f, entropies S, and specific heats at constant volume C_v at 298.15 K. Here, S and C_v were obtained from Eq. (2), i.e., $S(T)=-\partial F/\partial T$ and $C_v(T)=T\partial S/\partial T$.[38,39] As portrayed in Table I, calculation results for the bulk properties agree well with the experimental ones and are expected to confirm reasonable numerical precision for the energetic estimation through this work.

We show in Fig. 1 the calculated phonon dispersions for ZrB_2, NbB_2, and α-B bulk crystals. A gap region around 40 meV is exhibited by ZrB_2 and NbB_2 bulk crystals in Figs. 1(a) and 1(b), showing the atomic-mass difference between B and TM. The phonon modes above (lower) this gap can be assigned energetically to the B (TM) atoms. It is worth noting that the highest phonon modes by B-B are of about 100 meV in TMB_2 and about 146 meV in α-B. The highest energy phonon mode corresponds to the shortest B-B stretching mode in TMB_2 and α-B crystals, the bond lengths of which are, respectively, about 180 and 167 pm. These energies agree well with other calculations presented in the literature.[40,41]

The calculated phonon energies and electronic DOS at the Fermi level for the bulks are used to determine a possible scope of $\Delta\mu_B$ at each temperature via $\mu_B^{bulk}(T)$ and $\Delta H_f(T)$ in Sec. III F.

B. Preliminary surface MD simulations

In Fig. 2, the initial and final surface configurations of the MD simulations with several boron coverages are displayed. Here, we defined the value for 1 monolayer (ML) coverage as consisting of a complete 1×1 structure surface. Although the MD time steps of 2.9 fs used here are only about one-tenth of the highest phonon frequency attributed to B-B bonds [approximately 28 fs (146 meV) for α-B and 41 fs (100 meV) for TMB_2, as shown in Fig. 1], they are useful to evolve the dynamics both efficiently and correctly.

The results of preliminary MD simulations presented the following features. (1) Even after annealing at 2500 K, the Zr and substrate B atoms apparently remained in their initial sites, although the surface B atoms moved well on the surface. Most of them sit on the threefold hollow sites of the underlying Zr layer. (2) The surface B atoms tend to produce aggregates in most coverages of B. (3) A boron atom can rise on the surface B layer apart from the Zr layer, as presented in Figs. 2(a)–2(c). In particular, in boron-rich conditions of 2/3 ML-B and 1 ML-B, *umbrella*like B_7 clusters appear on the surface, as shown in the dashed circles in Figs. 2(a) and 2(b).

Feature (1) is expected to be consistent with a high melting point of bulk ZrB_2 (>3300 K). Features (1) and (2)

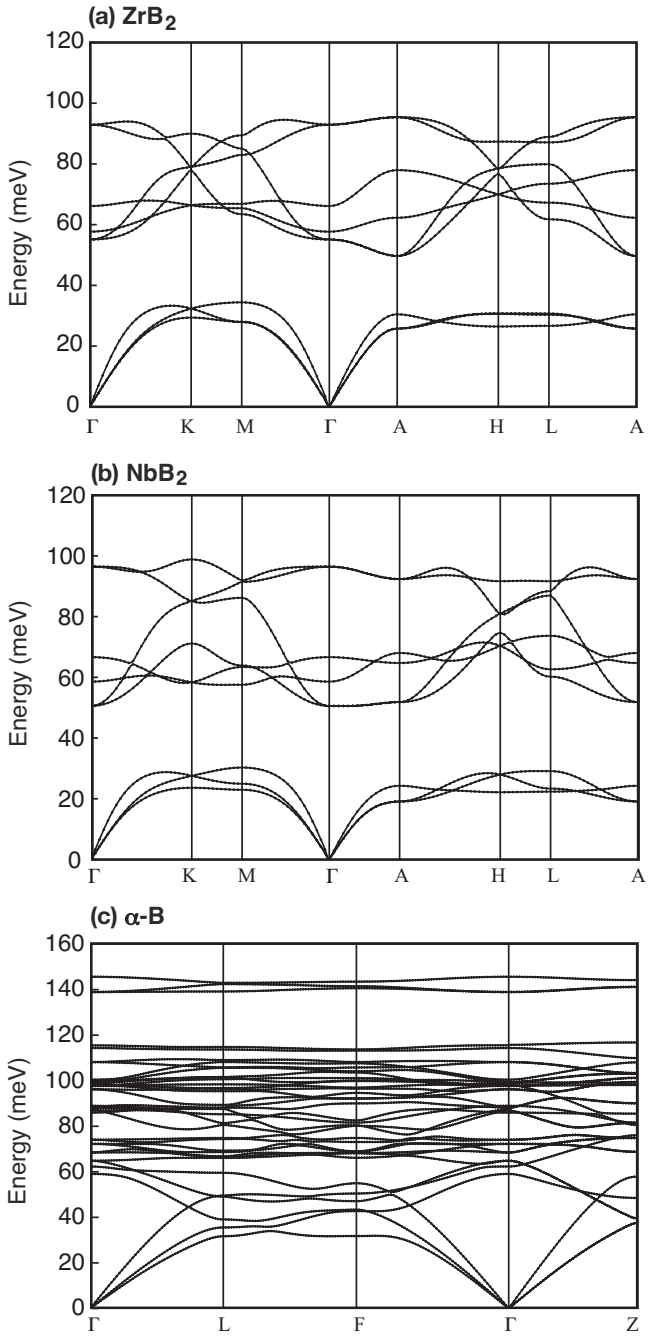

FIG. 1. Calculated phonon dispersions for (a) ZrB_2, (b) NbB_2, and (c) α-B bulk crystals.

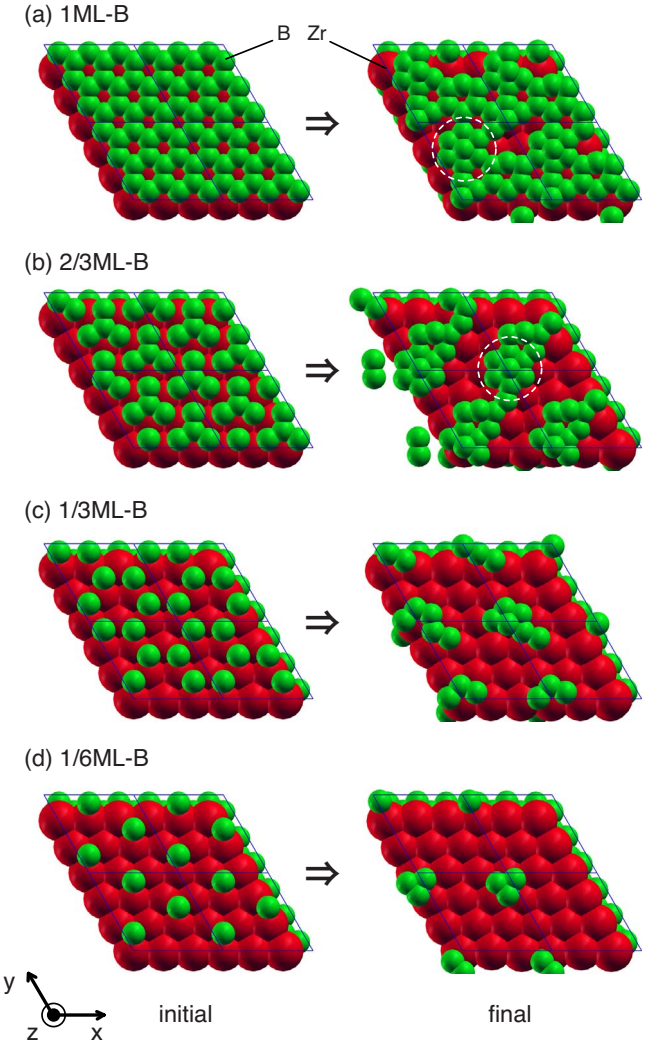

FIG. 2. (Color online) Molecular-dynamics simulation results of the $ZrB_2(0001)$ 3×3 surface units for (a) 1 ML-B, (b) 2/3 ML-B, (c) 1/3 ML-B, and (d) 1/6 ML-B. The initial (left-hand side) and final (right-hand side) configurations are displayed as 6×6 surface units for ease of visualization of the local structures around the 3×3 periodic boundary. The graphics were produced using XCRYSDEN software (Ref. 42).

suggest that, even in a boron-poor experimental condition, the surface boron atoms might make local aggregations. That is, the 1×1 Zr phase and boron-rich phase might coexist on a real $ZrB_2(0001)$ surface in most coverages of B. Moreover, in the (local) boron-rich area, those of the local structures offered by feature (3) should appear in the $\sqrt{3}$ phase.

C. Surface-formation free energy

We obtained final structures of several types after the structure optimization from the various initial $\sqrt{3}$ surface configurations. Figure 3 shows the lowest energy structures found in the present work for each B or Zr coverage. The $\sqrt{3}$ optimized structures of 1/6 ML-B, 1/3 ML-B, 2/3 ML-B, and 1 ML-B coverages [Figs. 3(d), 3(e), 3(g), and 3(i)] differ from the preliminary MD results of the respective boron coverages shown in Fig. 2. However, this discrepancy is not surprising because the $\sqrt{3}$ periodic boundary condition engenders an optimized structure of only $\sqrt{3}$ (or 1×1) periodicity, even for *incompatible* coverages.

In general, if an incompatible coverage with a specified surface structure happens in an experiment, a phase separation might occur as described in Sec. III B. Alternatively, the substrate, as a thermodynamic particle reservoir, might exchange the atoms with the surface to some extent until a *compatible* coverage and/or structure is established. In this work, the compatible coverages and structures can be elucidated by the surface-formation free energy and a possible scope of the chemical potential of boron or TM.

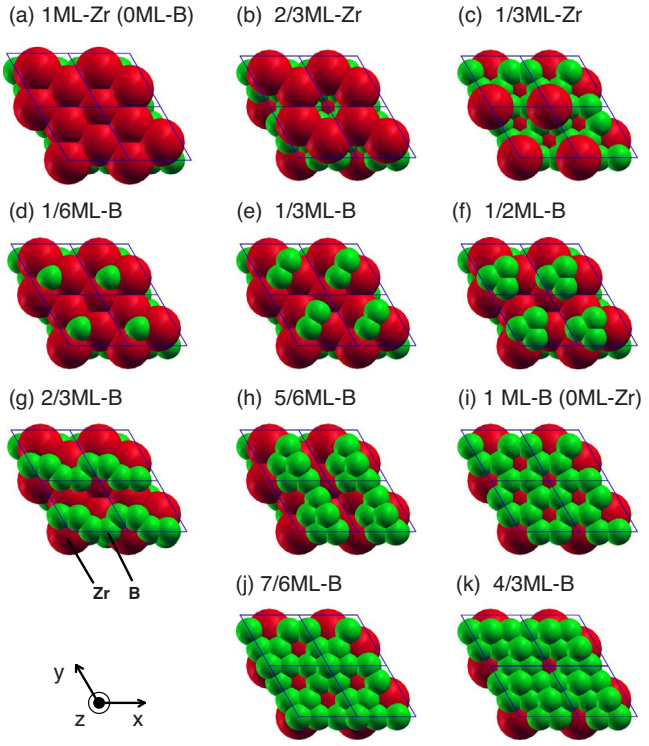

FIG. 3. (Color online) Calculated $ZrB_2(0001)$-$\sqrt{3}$ optimized structures for various boron coverages. These surface structures are displayed as a $2\sqrt{3}\times 2\sqrt{3}$ surface unit. (a) 1×1 Zr (close packed), (b) Zr honeycomb (Zr surface defect), (c) Zr on a hollow site of boraphene, (d) B on a Zr hollow site, (e) B dimer (three domains), (f) B trimer, (g) rumpled zig-zag B-chain (three domains), (h) adatom B on a fourfold site of B (three domains), (i) 1×1 B (boraphene), (j) adatom B on a hollow site of boraphene, and (k) same as (j) but two adatoms B.

Figure 4(a) shows the surface-formation free energy γ_0 for the lowest energy $ZrB_2(0001)$ surfaces at typical coverages of B or Zr. The lowest γ_0 among the examined coverages in Fig. 4(a) indicates that the 1×1 Zr phase with 1 ML-Zr and the $\sqrt{3}$ phase with 7/6 ML-B are most stable in the possible scope of $\Delta\mu_B$. We show also in Fig. 4(b) γ_0 of the several $NbB_2(0001)$-$\sqrt{3}$ models for comparison with the $ZrB_2(0001)$ results. The 1×1 boraphene surface has been well identified experimentally for the $NbB_2(0001)$ surface among them.[13] In contrast to the $ZrB_2(0001)$ system, the surface-formation free energy for the $\sqrt{3}$ phase with 7/6 ML-B on $NbB_2(0001)$ appears to be higher than that of the 1×1 phase in the B-rich region. Consequently, Fig. 4 leads us to the conclusion that surface boron phases of two types exist on $TMB_2(0001)$ in the B-rich condition: $\sqrt{3}$ and 1×1 boraphenes on the $ZrB_2(0001)$ and $NbB_2(0001)$, respectively, as presented schematically in Figs. 5(a) and 5(b). It is worth noting that the sixfolded adatom B found in the $\sqrt{3}$ boraphene has already been observed as the *umbrella* B_7 cluster in the aggregation in Figs. 2(a) and 2(b), indicating that preliminary MD simulations with large area are expected to provide useful hints for unknown surface structures. This local structure is also found at the 4/3 ML-B coverage surface [Fig. 3(k)], but this surface has much higher γ_0 than the 7/6 ML-B $\sqrt{3}$ boraphene surface [Fig. 4(a)]. Consequently,

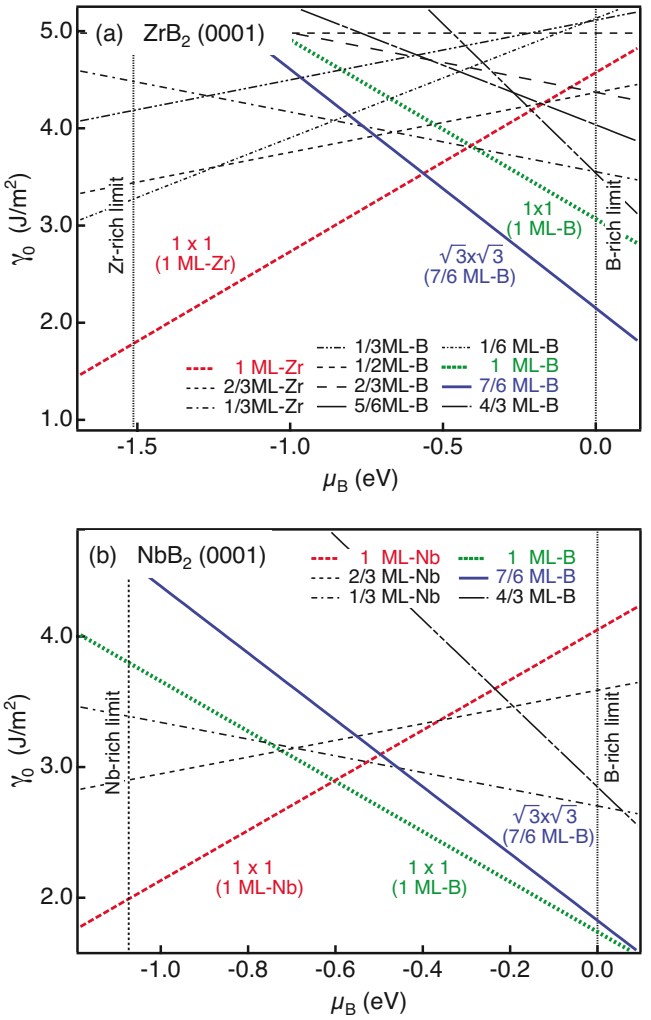

FIG. 4. (Color online) Calculated surface-formation free energy γ_0 for (a) $ZrB_2(0001)$ and (b) $NbB_2(0001)$ as a function of the chemical potential $\Delta\mu_B=\mu_B-\mu_B^{bulk}$.

the surface at a coverage of 4/3 ML-B (and also other incompatible coverages) is rejected for a possible $\sqrt{3}$ surface within the scope of $\Delta\mu_B$.

The 7/6 ML-B $\sqrt{3}$ boraphene sheet on $ZrB_2(0001)$ consists of $\sqrt{3}$-adatom B and the underlying B-honeycomb (quasi-1×1) boraphene. This structure analysis suggests that a small amount of the adatom B (1/6 ML) helps to stabilize the electron-deficient 1×1 surface boraphene on the group-IV Zr layer that has less electron-donation ability than a group-V Nb layer. However, the stabilization mechanism of $\sqrt{3}$ phase is not simply described by the charge-transfer picture that can explain the stability boundary of the 1×1 boraphene phase on $TMB_2(0001)$. These stabilization mechanisms are discussed from the electronic-structure perspective in the following section.

D. DOS analysis of boraphene structures

Partial DOS for the boraphene surface models elucidate the origin of the stability of the 1×1 and $\sqrt{3}$ boraphene structures on $TMB_2(0001)$. Figure 6 exhibits partial DOS to

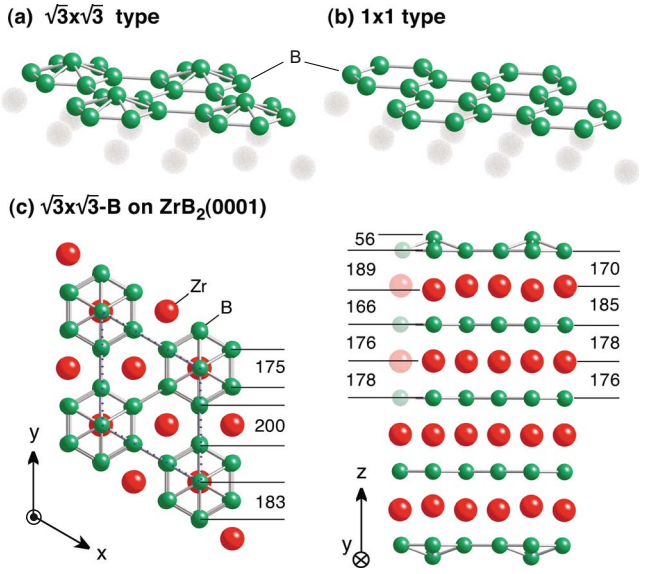

FIG. 5. (Color online) Boraphene structures. (a) $\sqrt{3}$ phase (7/6 ML-B) in which a $\sqrt{3}$ B adatom is located at the center of every three B honeycombs. (b) 1×1 phase (1 ML-B). (c) Top and side views of the optimized $ZrB_2(0001)$-$\sqrt{3}$ model, respectively, showing B-B bond lengths and atomic distances along the z axis (in pm).

the outermost B layer and their p_z orbitals. Although the 1×1 boraphene on $ZrB_2(0001)$ [Fig. 6(b)] exhibits a quite similar partial DOS to that on $NbB_2(0001)$ [Fig. 6(a)], it has a fractionally occupied peak of the surface B p_z orbital components around ϵ_f that might render the surface system unstable [see the peaks denoted by asterisk in Figs. 6(a) and 6(b)]. This is expected to be the main reason why a group-V $TMB_2(0001)$ surface exhibits the 1×1 boraphene and a group-IV $TMB_2(0001)$ does not. Namely, within a rigid-band picture, the group-V(IV) TM layer can (cannot) provide sufficient electrons to the 1×1 boraphene to stabilize it with filling surface B p_z: bonding π orbitals.

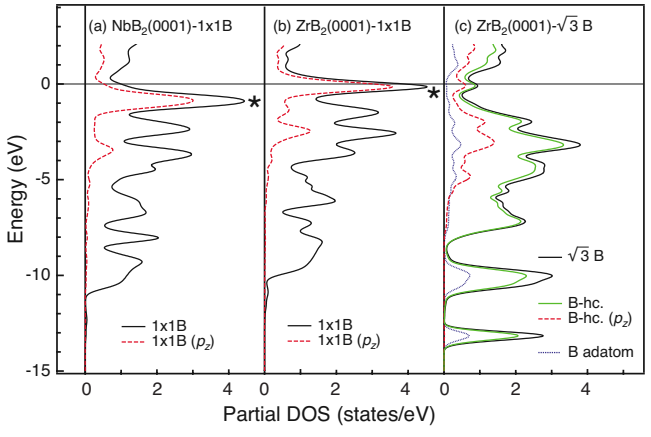

FIG. 6. (Color online) Calculated partial electronic DOS of each $\sqrt{3}$ surface unit cell: (a) $NbB_2(0001)$ 1×1 B, (b) $ZrB_2(0001)$ 1×1 B, and (c) $ZrB_2(0001)$ $\sqrt{3}$ B. Large peaks (asterisk) around the Fermi level ($\epsilon_f\equiv0$) in 1×1 B surfaces [(a) and (b)] mainly consist of the p_z orbital component of surface 1×1 B atoms. The B-hc in (c) denotes the B-honeycomb (quasi-1×1) component found in the $\sqrt{3}$ boraphene.

On the other hand, the $\sqrt{3}$ boraphene [Fig. 6(c)] shows no large peak at ϵ_f and exhibits low-energy DOS around -10 and -13 eV. The partial DOS of the $\sqrt{3}$ boraphene differs greatly from the 1×1 boraphenes; the partial DOS of the B adatom in low-energy region suggests significant interaction of the B adatom and the underlying B-honeycomb sheet. Therefore, the $\sqrt{3}$ boraphene stability should not be interpreted by the simple electron transfer from the B adatom to the 1×1 boraphene. Two B-B bond lengths of 175 and 200 pm in the underlying B-honeycomb layer [Fig. 5(c)] are expected to reflect this significant interaction effect also. In fact, these bond-length modifications appear also in the underlying B-honeycomb phonon modes, as shown in the next section.

In Fig. 5(c), the structural unit of umbrellalike B_7 has a B-B bond length of about 180 pm and the B_7 structural units are mutually interconnected with a distance of 200 pm. Similar intra-B-B and inter-B-B bond lengths can be found in α-B crystal, typical borides and boron hydrides.[29,43] The above DOS and structure analyses suggest that the $\sqrt{3}$ structure is preferably interpreted by an inherent bonding in itself rather than by the simple modification of the 1×1 boraphene with a B adatom.

E. Phonon dispersion

In Fig. 7, the calculated phonon-dispersion relations of the $TMB_2(0001)$ surfaces are shown. These dispersion curves are drawn with the weight of the surface B atoms in the wave vector parallel to the surface $\boldsymbol{q}$ in gray scale for comparison to the experimental-data plots by the HR-EELS observation.[13,18]

The calculated phonon dispersions show excellent agreement with the HR-EELS data and reveal the following features: both $\sqrt{3}$ and 1×1 boraphenes exhibit the phonon modes lie in the energy are 40–50 meV [Figs. 7(a) and 7(b)], which is the gap region both in TMB_2 bulks [Figs. 1(a) and 1(b)] and the metal-terminated surface system [Fig. 7(c)]. In addition to these phonon modes, the $\sqrt{3}$ boraphene correctly yields phonon modes around 80 meV at $\bar{\Gamma}$ point and greater than 100 meV around $\bar{K}$.

In Fig. 8, some of surface phonon modes at $\bar{\Gamma}$ point focusing on the B-honeycomb structures are shown. Surface longitudinal optical (LO) mode assigned to an almost stretching vibration of the shortest B-B bond in $\sqrt{3}$ boraphene [Fig. 8(a)] shows much higher phonon energy than the highest LO mode of the surface 1×1 boraphene [Fig. 8(e)], reflecting the difference between the B-B bond lengths of 175 and 179 pm. Although the phonon-energy difference between the z-displaced (normal to the surface) optical modes of the B-honeycombs shown in Figs. 8(b) and 8(f) are less than 2 meV, the z-displaced acoustic (ZA) and surface longitudinal acoustic (LA) modes of the $\sqrt{3}$ boraphene [Figs. 8(c) and 8(d)] exhibit lower energies of >3 meV than the respective ZA and LA modes for the 1×1 boraphene [Figs. 8(g) and 8(h)]. The LA softening is well explained with the mass change of the boraphene: adding one boron atom can decrease the frequency by $\sqrt{6/7}$. In fact, the frequency ratio (38.72 meV/41.94 meV) is almost identical to $\sqrt{6/7}$. The

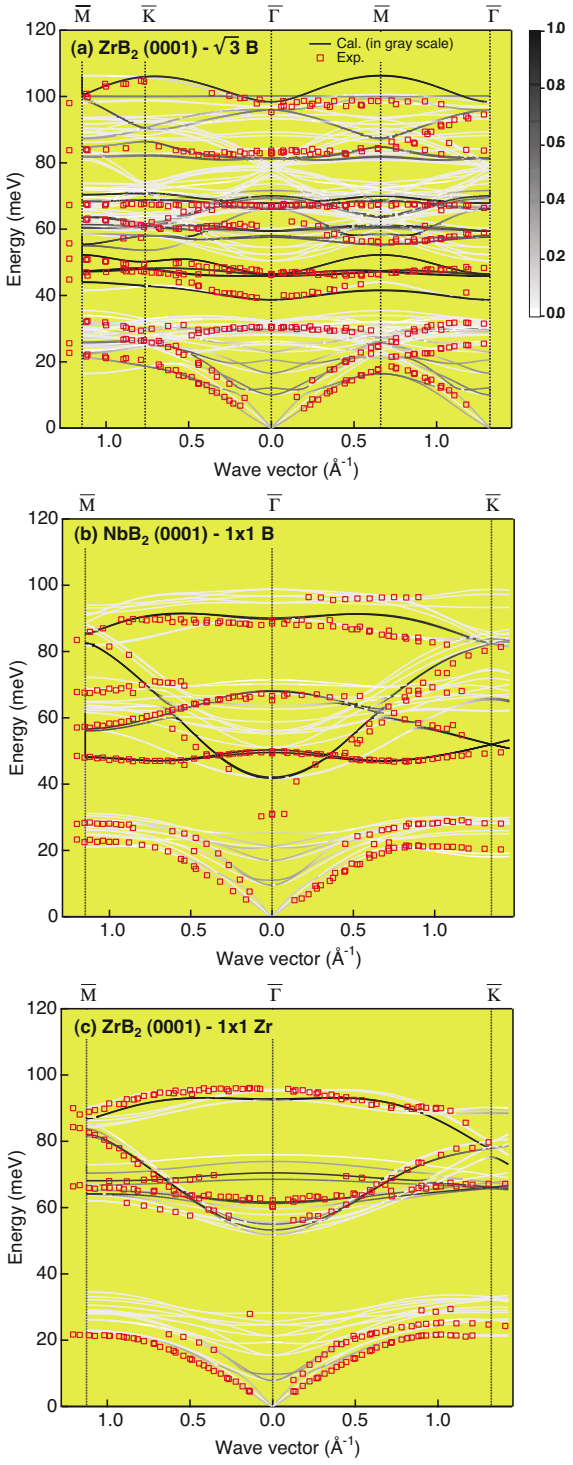

FIG. 7. (Color online) Calculated phonon-dispersion relations of $TMB_2(0001)$ slabs. The dispersion curves are drawn with the weight of the surface B atoms in the wave vector parallel to the surface $\boldsymbol{q}$ in gray scale for comparison with the experimental data plots (□) by HR-EELS (Refs. 13 and 18). (a) $\sqrt{3}$ boraphene on $ZrB_2(0001)$, (b) 1×1 boraphene on $NbB_2(0001)$, and (c) 1×1 Zr on $ZrB_2(0001)$ surfaces. In the 1×1 Zr surface [(c)], the second layer's (i.e., first boron layer's) phonon-dispersion curves are displayed. Regions of $\overline{M}$-$\overline{K}$-$\overline{\Gamma}$ (right-hand side) and $\overline{\Gamma}$-$\overline{M}$-$\overline{\Gamma}$ (left-hand side) in (a) correspond to $\overline{M}$-$\overline{\Gamma}$ and $\overline{\Gamma}$-$\overline{K}$ regions in the 1×1 systems [(b) and (c)], respectively.

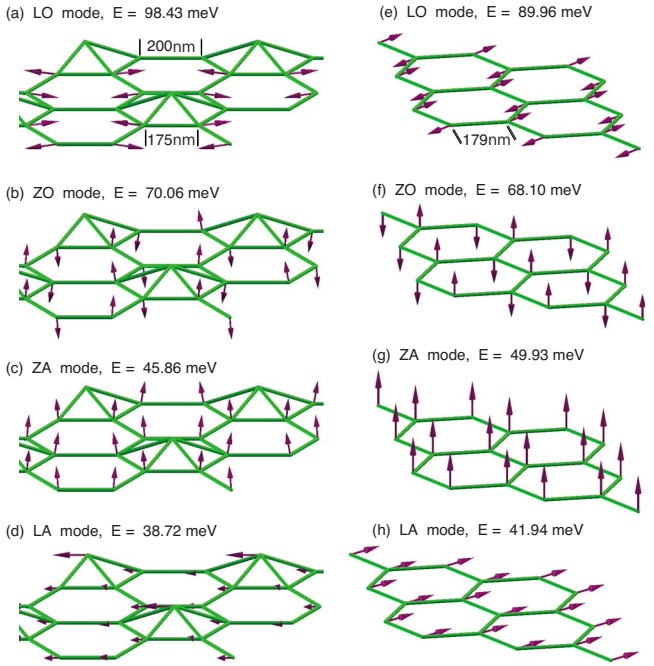

FIG. 8. (Color online) Some of surface B-honeycomb phonon modes at $\bar{\Gamma}$ point ($\boldsymbol{q}=0$) for $\sqrt{3}$ boraphene on $ZrB_2(0001)$ [(a)–(d)] and 1×1 boraphene on $NbB_2(0001)$ [(e)–(h)], respectively. The $\sqrt{3}$ phonon mode names are denoted with particular emphasis on the boraphene honeycombs (see text).

adatom is positioned on top of the Zr. Therefore, the contribution of this Zr-B bond is expected to be weak in the LA mode. On the other hand, as portrayed in Fig. 8(c), the adatom does not vibrate in the ZA mode, so the softening of the ZA mode cannot be explained by the mass change. The ZA softening can be associated with weaker binding between the surface $\sqrt{3}$ boraphene and the Zr layer than that of the surface 1×1 boraphene and the Nb layer in the respective systems. It also appears in the surface interlayer distances: the surface interlayer distance between the $\sqrt{3}$ boraphene and Zr layers (176 pm as an average value) is 6% larger than the 1×1 boraphene-Nb layer distance (166 pm). In the phonon modes around 30, 55–60, and 80 meV at the $\bar{\Gamma}$ point in Fig. 7(a), it is most likely that folded-backlike modes appear from $\overline{K}$ point in the 1×1 BZ in addition to the inherent modes of $\sqrt{3}$ boraphene because the $\overline{K}$ point of the 1×1 BZ is folded into the $\bar{\Gamma}$ point in the $\sqrt{3}$ BZ (see Fig. 7). That is, the motions of these modes might be associated with those of the 1×1 boraphene at $\overline{K}$ in Fig. 7(b).

Previously, we proposed[18] a $\sqrt{3}$ surface model at the coverage of 1/3 ML-Zr [as shown in Fig. 3(c)] as the simplest model based on experimental results obtained for the B coverage by the x-ray photoelectron spectroscopy (XPS) and 1×1 boraphene phonon modes in the energy range of 40–50 meV (gap modes). The present calculation results revealed the new $\sqrt{3}$ boraphene phase with 7/6 ML-B [Fig. 5(a)], which is consistent with the high-energy phonon modes in addition with the gap modes. The coverage of 7/6 ML-B for the $\sqrt{3}$ boraphene is slightly larger than the experimental estimation at 0.8 ± 0.2 ML probably because a small amount of the 1×1 Zr phase coexists with the $\sqrt{3}$ structure, as de-

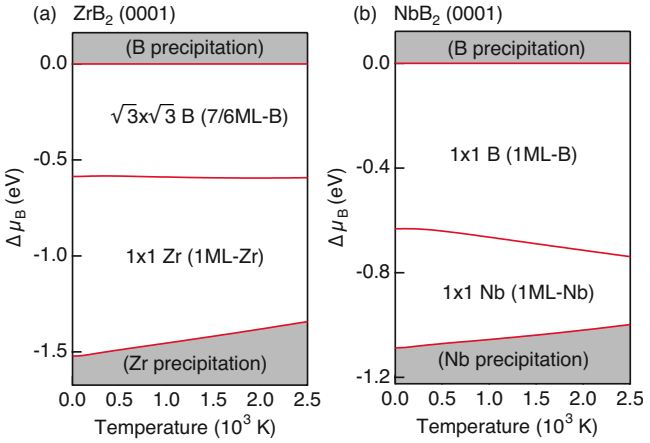

FIG. 9. (Color online) Calculated phase diagrams for (a) $ZrB_2(0001)$ and (b) $NbB_2(0001)$ surfaces.

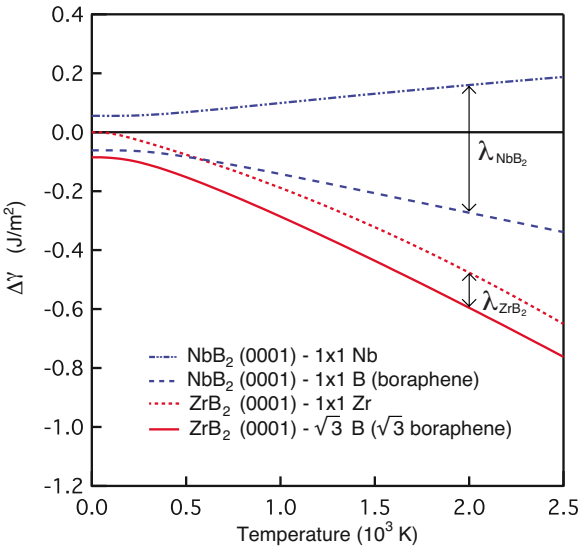

FIG. 10. (Color online) Surface-formation free-energy contribution of phonons and electrons, $\Delta\gamma(T)=\gamma(T,\Delta\mu_B)-\gamma_0(\Delta\mu_B)$. λ denotes an energy difference of $\Delta\gamma$ between the metal and boron surfaces.

scribed in Secs. III B and III C. The optimized $\sqrt{3}$ structure in Fig. 5(c) shows a slight rumpling of the Zr atoms along the z axis in addition to the surface boron reconstruction, which might contribute to the sharp and strong $\sqrt{3}$ reflections in the reflection high-energy electron-diffraction measurement.[18]

F. Phase diagram

Finally, we specifically examine the thermodynamic analysis of the present systems. In Fig. 9, we present the calculated phase diagrams for the $ZrB_2(0001)$ and $NbB_2(0001)$ surfaces derived from the surface-formation free energy $\gamma(T,\Delta\mu_B)$ for the typical experimental temperatures of 0–2500 K. The present phase diagrams do not involve effects of phase transitions in B or Zr bulks because their effect is limited (no phase transition is known for Nb in this temperature range). In this temperature range, the bulk boron shows the α-to-β phase transition at a temperature of 1400 K and melts at a temperature (T_{mp}) of 2500 K. For bulk zirconium, a phase transition occurs at 1135 K and T_{mp} =2100 K. The energy correction for bulk boron is less than about 100 meV, even at around 2500 K, as inferred from Ref. 44. Regarding bulk zirconium, the correction should range within the order of 70–110 meV at 2000 K from Refs. 45 and 46. Consideration of the corrections described above does not markedly modify the phase boundaries.

As Fig. 9 shows, the 1×1 Zr and 1×1 boraphene surfaces are apparently thermodynamically favorable in $ZrB_2(0001)$ and $NbB_2(0001)$, respectively, from the viewpoint of the possible scope of $\Delta\mu_B$. This result should correspond to the known fact that a group-IV(V) $TMB_2(0001)$ surface would be terminated with the TM(B) layer in typical surface-cleaning treatments at a high temperature in a vacuum.[11,13,14,18] The desorption effect of the surface B or TM atoms during the surface-cleaning treatment is explainable by a variation of $\Delta\mu_B$ in these phase diagrams. In $ZrB_2(0001)$, the relative region of the $\sqrt{3}$ boraphene phase expands with increasing temperature because the 1×1 Zr region gradually decreases at higher temperatures, as portrayed in Fig. 9(a). A similar growth of the 1×1 boraphene region is also found in $NbB_2(0001)$ in Fig. 9(b).

Figure 10 shows the contribution of phonons and electrons to the surface-formation free energy, $\Delta\gamma=\gamma-\gamma_0$, which is a function of temperature. A typical energy ratio F^{el}/F^{ph} is less than ~3% in the present calculation, and therefore the phonon freedom mainly contributes to $\Delta\gamma$, as generally expected.[22] $\Delta\gamma$ for the ZrB_2 surfaces vary up to about 0.7 J/m^2 within our temperature range as shown in Fig. 10. However, the energy difference between the surfaces types (λ_{ZrB_2}) retains a similar value of about 0.1 J/m^2 at each temperature. This leads the phase boundary between the 1×1 Zr and $\sqrt{3}$ boraphene phases to form a nearly flat line around $\Delta\mu_B\sim-0.6$ eV with respect to temperature in Fig. 9(a). A slope of the phase boundary between the 1×1 Nb and boraphene phases in Fig. 9(b) is originated from a variation of λ_{NbB_2} with temperature as portrayed in Fig. 10, while $\Delta\gamma$ for the NbB_2 surfaces exhibits a smaller variance than those for the ZrB_2 surfaces. Consequently, the surface-formation free energy with the contribution of F^{el} and F^{ph} reveals that the thermodynamically favorable regions of the boraphenes are slightly larger at higher temperatures as portrayed in Fig. 9.

IV. SUMMARY

Results of this study revealed the $\sqrt{3}$ boraphene structure in addition to the well-known 1×1 boraphene on $TMB_2(0001)$ using the first-principles MD simulations and the surface-formation free-energy calculations. The full-phonon calculations based on the density-functional perturbation theory were performed for the $TMB_2(0001)$ surfaces and the bulks of TMB_2, α-B, Zr, and Nb. The calculated bulk properties of the structures, the heats of formation, entropies, and specific heats well reproduce the experimental ones found in the relevant literature. For the TMB_2 surfaces, ex-

cellent agreement of the full-phonon dispersion calculations with the HR-EELS measurements has been presented. Analyses of the electronic structure elucidated the origin of the 1×1 boraphene stability on the $TMB_2(0001)$ surfaces within a rigid-band picture: the group-V(IV) TM layer can (cannot) provide sufficient electrons to the 1×1 boraphene to stabilize it with filling surface B p_z (bonding π orbitals). Regarding the $\sqrt{3}$ boraphene, the significant interaction of the B adatom and the underlying B honeycomb was found in the partial DOS. That interaction is expected to cause the short B-B bonds that exhibit the high phonon-frequency modes. The surface-formation free-energy calculations involving temperature effects based on the Sommerfeld theory and the harmonic approximation have revealed the thermodynamically favorable region of both $\sqrt{3}$ and 1×1 boraphenes.

ACKNOWLEDGMENTS

All calculations were performed using workstations (MacPro; Apple Computer, Inc.) and a numerical materials simulator (SR11000; Hitachi, Ltd.) at our institute (NIMS). One of the authors (S.S.) wishes to thank K. Kobayashi, M. Arai, J. Inoue, Y. Miwa, S. Inoue, and S. Otani (NIMS) for their support and encouragement during this work.

[1] W. Gordon Jr. and S. B. Soffer, J. Phys. Chem. Solids **36**, 627 (1975).
[2] B. Post, *Boron, Metal-Boron Compounds and Boranes* (Wiley, New York, 1966).
[3] J. Nagamatsu, N. Nakagawa, T. Muranaka, Y. Zenitani, and J. Akimitsu, Nature (London) **410**, 63 (2001).
[4] A. K. Geim and K. S. Novoselov, Nature Mater. **6**, 183 (2007).
[5] N. Bonini, M. Lazzeri, N. Marzari, and F. Mauri, Phys. Rev. Lett. **99**, 176802 (2007).
[6] A. H. Castro Neto, F. Guinea, N. M. R. Peres, K. S. Novoselov, and A. K. Geim, Rev. Mod. Phys. **81**, 109 (2009).
[7] M. Arai and Y. Hatsugai, Phys. Rev. B **79**, 075429 (2009).
[8] T. Aizawa, R. Souda, S. Otani, Y. Ishizawa, and C. Oshima, Phys. Rev. Lett. **64**, 768 (1990).
[9] J. C. Meyer, A. Chuvilin, G. Algara-Siller, J. Biskupek, and U. Kaiser, Nano Lett. **9**, 2683 (2009).
[10] H. Kawanowa, R. Souda, S. Otani, and Y. Gotoh, Phys. Rev. Lett. **81**, 2264 (1998).
[11] W. Hayami, R. Souda, T. Aizawa, and T. Tanaka, Surf. Sci. **415**, 433 (1998).
[12] C. L. Perkins, R. Singh, M. Trenary, T. Tanaka, and Y. Paderno, Surf. Sci. **470**, 215 (2001).
[13] T. Aizawa, W. Hayami, and S. Otani, Phys. Rev. B **65**, 024303 (2001).
[14] K. Yamamoto, K. Kobayashi, H. Kawanowa, and R. Souda, Phys. Rev. B **60**, 15617 (1999).
[15] Y. Han, Y. Dai, D. Shu, J. Wang, and B. Sun, J. Phys.: Condens. Matter **18**, 4197 (2006).
[16] T. Aizawa, S. Suehara, S. Hishita, S. Otani, and M. Arai, Phys. Rev. B **71**, 165405 (2005).
[17] *Boron and Refractory Borides*, edited by V. I. Matkovich (Springer-Verlag, Berlin, 1977).
[18] T. Aizawa, S. Suehara, S. Hishita, and S. Otani, J. Phys.: Condens. Matter **20**, 265006 (2008).
[19] R. M. Martin, *Electronic Structure* (Cambridge University Press, United Kingdom, 2005).
[20] S. Baroni, S. de Gironcoli, A. D. Corso, and P. Giannozzi, Rev. Mod. Phys. **73**, 515 (2001).
[21] N. W. Ashcroft and N. D. Mermin, *Solid State Physics* (Thomson Learning, United Kingdom, 1976).
[22] C. Kittel, *Introduction to Solid State Physics* (Wiley, New York, 1986).
[23] J. P. Perdew and Y. Wang, Phys. Rev. B **45**, 13244 (1992).
[24] P. Giannozzi *et al.*, http://www.quantum-espresso.org
[25] D. Vanderbilt, Phys. Rev. B **41**, 7892 (1990).
[26] H. J. Monkhorst and J. D. Pack, Phys. Rev. B **13**, 5188 (1976).
[27] N. Marzari, D. Vanderbilt, A. DeVita, and M. C. Payne, Phys. Rev. Lett. **82**, 3296 (1999).
[28] T. Tanaka, Y. Ishizawa, E. Bannai, and S. Kawai, Solid State Commun. **26**, 879 (1978).
[29] G. Will and B. Kiefer, Z. Anorg. Allg. Chem. **627**, 2100 (2001).
[30] J. Goldak, L. T. Lloyd, and C. S. Barrett, Phys. Rev. **144**, 478 (1966).
[31] A. Pialoux, M. L. Joyeux, and G. Cizeron, J. Less-Common Met. **87**, 1 (1982).
[32] R. B. Kotelinikov, S. N. Bashlykov, Z. G. Galiakbarov, and A. I. Kashtanov, *Special Refractory Metals and Compounds* (Metallurgia, Moscow, 1969) (in Russian).
[33] J. Samuel and J. Schneider, *ASM Engineering Materials Handbook* (ASM International, Materials Park, OH, 1991), Vol. 4.
[34] L. Topor and O. J. Kleppa, J. Chem. Thermodyn. **17**, 1003 (1985).
[35] R. Schumm, D. Wagman, S. Bailey, W. Evans, and V. Parker, NBS Tech. Note **270**, 1 (1973).
[36] J. D. Cox, D. D. Wagman, and V. A. Medvedev, *CODATA Key Values for Thermodynamics* (Hemisphere, New York, 1989).
[37] A. S. Bolgar, M. I. Serbova, T. I. Serebryakova, L. P. Isaeva, and V. V. Fesenko, Powder Metall. Met. Ceram. **22**, 207 (1983).
[38] $S=\frac{(\pi k_B)^2}{3}D(\epsilon_f)T+k_B\Sigma_s[\frac{\hbar\omega_s}{2k_BT}\coth\frac{\hbar\omega_s}{2k_BT}-\ln(2\sinh\frac{\hbar\omega_s}{2k_BT})]$
[39] $C_v=\frac{(\pi k_B)^2}{3}D(\epsilon_f)T+k_B\Sigma_s(\frac{\hbar\omega_s}{2k_BT})^2\sinh^{-2}\frac{\hbar\omega_s}{2k_BT}$
[40] K. Shirai and H. Katayama-Yoshida, Physica B **263-264**, 791 (1999).
[41] P. P. Singh, Phys. Rev. B **69**, 094519 (2004).
[42] A. Kokalj, Comput. Mater. Sci. **28**, 155 (2003).
[43] W. Hayami, T. Tanaka, and S. Otani, J. Phys. Chem. A **109**, 11975 (2005).
[44] A. Masago, K. Shirai, and H. Katayama-Yoshida, Phys. Rev. B **73**, 104102 (2006).
[45] F. Willaime and C. Massobrio, Phys. Rev. Lett. **63**, 2244 (1989).
[46] C. V. Greeff, Modell. Simul. Mater. Sci. Eng. **13**, 1015 (2005).